A conceptual design of two-stream alkali-activated materials

Sun, Yubo; Mohan, Manu K.; Tao, Yaxin; Zhang, Yi; Van Tittelboom, Kim; Ye, Guang; De Schutter, Geert

DOI
10.1016/j.cemconcomp.2024.105485

Publication date
2024

Document Version
Final published version

Published in
Cement and Concrete Composites

Citation (APA)
Sun, Y., Mohan, M. K., Tao, Y., Zhang, Y., Van Tittelboom, K., Ye, G., & De Schutter, G. (2024). A conceptual design of two-stream alkali-activated materials. *Cement and Concrete Composites*, *148*, Article 105485. https://doi.org/10.1016/j.cemconcomp.2024.105485

Cement and Concrete Composites 148 (2024) 105485

Contents lists available at ScienceDirect

Cement and Concrete Composites

journal homepage: www.elsevier.com/locate/cemconcomp

A conceptual design of two-stream alkali-activated materials

Yubo Sun [a], Manu K. Mohan [a], Yaxin Tao [a], Yi Zhang [a,b], Kim Van Tittelboom [a], Guang Ye [a,c], Geert De Schutter [a,*]

[a] Magnel-Vandepitte Laboratory, Department of Structural Engineering and Building Materials, Ghent University, 9052, Ghent, Belgium
[b] Key Laboratory of Advanced Civil Engineering Materials of Ministry of Education, School of Materials Science and Engineering, Tongji University, Shanghai, China
[c] Microlab, Section of Materials and Environment, Faculty of Civil Engineering and Geosciences, Delft University of Technology, Stevinweg 1, 2628, CN Delft, the Netherlands

ARTICLE INFO

Keywords:
Two-stream AAMs
Rheology
Microstructure
Self-compacting
3D-printing

ABSTRACT

To properly control the reaction kinetics and fresh properties evolution in conventional alkali-activated materials (AAMs), a conceptual design of two-stream AAMs has been proposed in this study. This is achieved by dividing the solid and liquid components in AAMs, including blast furnace slag (BFS) and electric arc furnace slag (EFS) precursors, as well as aqueous sodium hydroxide and silicate activators into two separate streams A and B, where a very limited reactivity is expected in individual streams to ensure sufficient workability retention. Moreover, a final-stage intermixing is required to combine individual stream mixtures and trigger the major activation reaction. Fresh and hardened properties of combined mixtures were checked at different stages. The microstructure and reaction products were investigated to understand the strength development. Low dynamic rheological parameters and good workability retention have been detected in all individual stream mixtures, accompanied by limited exothermic heat flows after the initial dissolution confirmed by calorimetry tests. Further, Portland cement (PC) is partially blended into stream A to alter the early stiffening process in combined mixtures and meet various setting demands after intermixing. However, this might lead to a reduction in mechanical properties, associated with the formation of porous microstructures and an increase in the Ca/Si ratio in reaction products. Eventually, the conceptual design is validated in different scenarios including self-compacting and 3D-printing concrete applications.

1. Introduction

Due to the global climate change, the CO_2 emission induced by the cement industry has attracted great attention in recent years [1]. Great efforts have been made to develop new generations of alternative binding materials, aiming to mitigate the environmental impact of producing Portland cement (PC) [2,3]. Alkali-activated materials (AAMs) have been developed as a class of green alternative binders [4,5], which may provide nearly equivalent performance compared to PC [6–8]. The alkali-activation reaction takes place between solid aluminosilicate precursors and liquid alkaline activators [9]. After the initial wetting of precursors, various ionic species are dissolved into the pore solution to assemble amorphous reaction products through polymerization [10].

By using highly amorphous precursors such as ground granulated blast furnace slag (BFS) and metakaolin, rapid workability loss and short setting time have been frequently reported, in particular when sodium hydroxide and silicate are applied as the activator [11–13]. Such rapid setting has brought great challenges on the delivery and operation of AAMs during the fresh stage [14]. On the other hand, the inclusion of less reactive precursors [15,16] or activators with lower alkalinity (such as carbonate and sulfate activators [17–19]) might lead to a much delayed setting and strength development, which is also unfavored in practical applications. Various chemical admixtures have been developed, for use in combination with PC materials, as effective tools to alter the fresh properties and stiffening process, as among which superplasticizers (SPs), retarders, and accelerators [16]. However, many of the existing chemical admixtures developed for PC materials become much less effective in combination with AAMs due to the interaction with the aggressive alkaline environment [11,20,21]. Nevertheless, several types of retarding chemicals (e.g. phosphoric salts [22], organic acids [23,24], borax [25], as well as nano zinc oxide and zinc nitrate [26,27]) have been reported effective in decelerating the initial setting of AAMs. However, AAMs blended with retarders may exhibit

---

* Corresponding author.
E-mail address: geert.deschutter@ugent.be (G. De Schutter).

https://doi.org/10.1016/j.cemconcomp.2024.105485
Received 14 December 2023; Received in revised form 16 February 2024; Accepted 19 February 2024
Available online 23 February 2024
0958-9465/

less-satisfying early strength development [28], as a consequence of the long induction-stage reactions when using silicate activators [29]. Accordingly, an effective methodology to properly control the rheology and hardening process of fresh AAMs is still lacking, which significantly obstructs large-scale practical applications.

Moreover, the conventional cement industry has shown increasing demand of blending blast furnace slag (BFS) as supplementary cementitious materials in more recent years [30]. As the mainstream precursor on the market, the competitive application of BFS in PC mixtures has brought impetus of exploring other by-products as potential resources to produce AAMs, especially from the steel industry [31]. Compared to the conventional blast furnace technology, the electric arc furnace is currently more widely applied to produce steel out of scrap, as the steel industry is stepping from new steel-making into a recycling system [32–34]. It has been reported that the annual production of electric arc furnace slag (EFS) reached 18 million tons in Europe [35]. EFS has been applied as a supplementary material in the construction sector, such as aggregate in road, asphalt pavement, and concrete structures since the early 20th century [36,37]. As EFS is rich in aluminum and silica in composition, more recent studies have explored the possibility of using EFS as a substitute material in PC [34,38] and AAM binders [33,39,40]. Considering the low reactivity nature of EFS [41], it was applied as a secondary precursor in this study to produce AAMs, which will be further explained in section 2.

For these purposes, the concept of ‘two-stream AAMs’ has been proposed in this study. By making use of BFS and EFS as precursors, solid and liquid components in AAMs were divided into two separate streams, which were combined with a final-stage intermixing before casting, to achieve workability retention. By varying the mix design, fresh and hardened properties of individual streams and combined mixtures were checked at different stages. The microstructure and reaction products were investigated to understand the strength development. Finally, the two-stream AAMs were further validated with self-compacting and 3D-printing concrete applications.

2. Two-stream AAMs

To avoid the rapid dissolution and setting as a consequence of the contact between highly amorphous precursors and alkaline activators, the conventional AAMs are fitted into a two-stream system. The key components predominating the early activation reaction progress are divided into two separate streams to ensure a sufficient open time in practical applications.

As shown in Fig. 1, the concept of ‘two-stream AAMs’ is developed by re-distributing solid and liquid components in AAMs into different streams. In specific, stream A is designed to introduce the primary (highly reactive) aluminosilicate source into the system, where the solid precursor particles are dispersed in water with a very limited dissolution rate [42]. It has been proven that the conventional SPs, developed for PC materials, become much less effective in combination with AAMs due to the alkaline media [20]. By using water as the dispersant, it remains possible to further alter the fluidity of stream A with a few types of SPs. Meanwhile, stream B brings in the alkaline compound, consisting of a secondary precursor (with low initial reactivity or nearly alkali-inert in ambient conditions) and concentrated alkaline activators. Due to the limited reactivity of such precursors at ambient conditions, elevated temperature or microwave is normally required to promote the reaction progress and obtain early-stage curing [43]. At ambient conditions, sodium silicate activators play a similar role as SPs to disperse the solid particles at early stages [44,45], improving the fluidity in stream B. In each individual stream, the chemical reaction progresses very limited, whereas the major activation reaction begins only if the individual streams are in contact and intermixed with each other (Fig. 1). The conceptual design proposed will be validated with the in-house developed twin-pipe pumping system [46], where two individual mixtures could be intermixed with a helical static mixer integrated at the end of the pump before extrusion.

3. Experimental method

3.1. Materials

In this study, BFS and EFS were applied as precursors to prepare the mixtures in separate streams. BFS was provided by Ecocem Benelux B.V., with a density of 2890 kg/m^3. EFS was provided by Orbix N.V., having a density of 3250 kg/m^3. In addition, PC CEM I 52.5 N was applied to partially replace BFS and further modify the early stiffening process in the combined two-stream AAMs.

The morphology of BFS, EFS, and PC was visualized with a scanning electron microscope (SEM), as shown in Fig. 2. Angular particles with irregular shapes were observed in all samples. The chemical composition of BFS, EFS, and PC was determined by X-ray fluorescence (XRF) and loss on ignition (LOI) as illustrated in Table 1. In view of the heavy metal content, the potential leaching of applying EFS to produce AAMs has been discussed in a previous study [47]. The particle size distribution determined by laser diffraction is shown in Fig. 3. The mineralogical composition of the raw materials, detected by X-ray diffraction (XRD), is presented in Fig. 4. The mineral phase compositions of raw materials determined by quantitative XRD analysis (explained in detail in section 3.3.1) are summarized in Table 2. It should be noted that crystalline phases were hardly detected in BFS apart from the zincite, and thereby it was considered amorphous.

Sodium hydroxide and sodium silicate were combined as the activators in this study. Reagent-grade sodium hydroxide anhydrous pearls were provided by Brenntag N.V., and the sodium silicate solution (15% Na_2O, 30% SiO_2, and 55% water) was provided by PQ Corporation. As a conventional type of SP, polynaphthalene sulfonate (PNS) was applied in stream A mixtures to improve the fresh property, which was provided

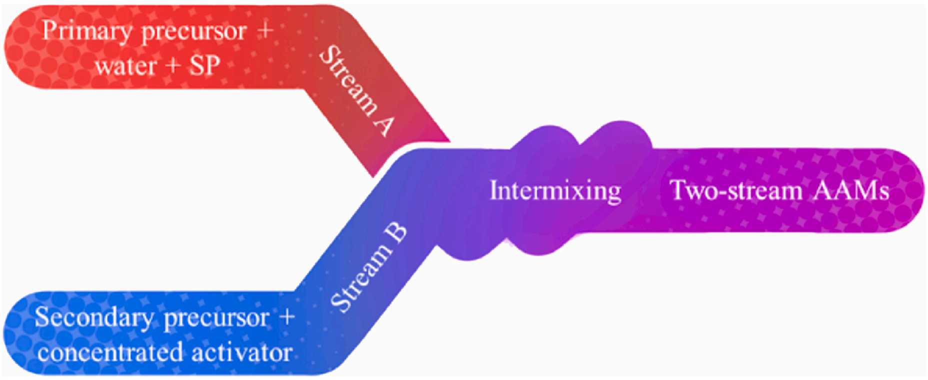

Fig. 1. Conceptual design of two-stream AAMs.

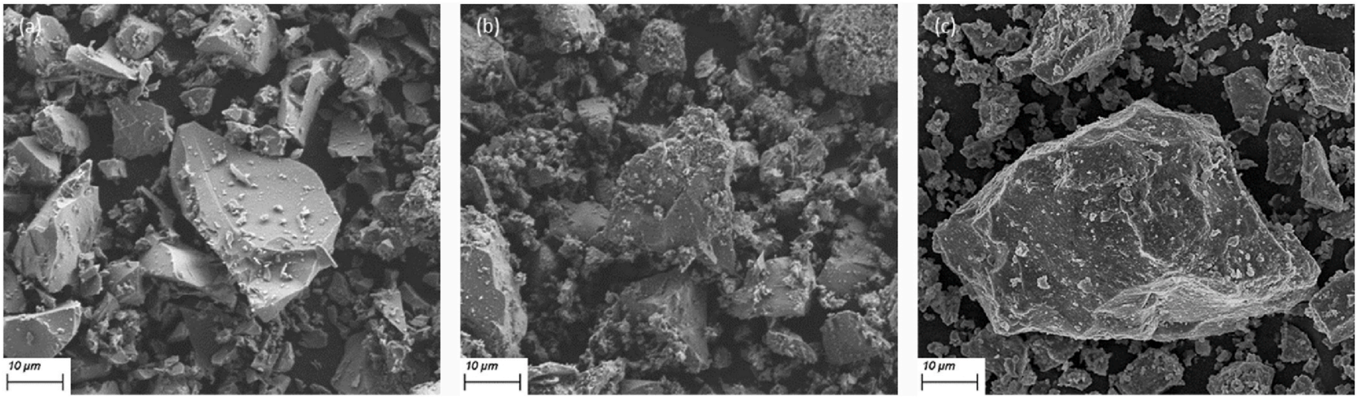

Fig. 2. Morphology of precursors visualized by SEM (a) BFS; (b) EFS; (c) PC.

Table 1
Chemical composition of BFS, EFS, and PC measured by XRF and LOI (mass %).

	CaO	SiO_2	Al_2O_3	MgO	SO_3	TiO_2	K_2O	Fe_2O_3	MnO	Cr_2O_3	Other	LOI[a]
BFS	40.9	31.1	13.7	9.16	2.31	1.26	0.69	0.40	0.31	–	0.17	0.10
EFS	44.2	28.0	6.3	4.41	0.49	1.64	–	2.04	2.65	9.9	0.37	0.86
PC	66.2	17.6	5.14	0.95	4.71	0.33	0.41	3.85	0.08	0.02	0.71	1.40
Sand	0.09	96.78	2.54	0.10	–	–	0.09	0.06	–	–	0.34	–

[a] LOI measured by TG analysis at 950 °C.

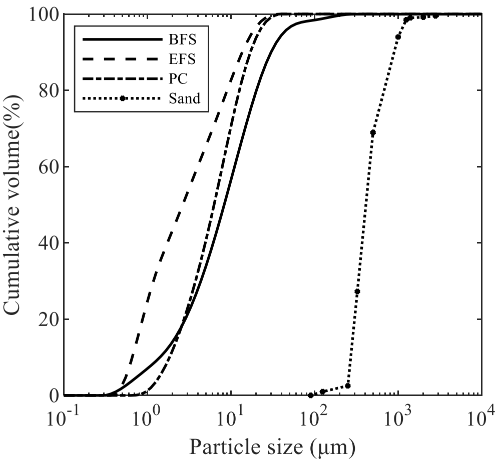

Fig. 3. Particle size distribution of the BFS, EFS, PC, and sand used in this study.

by BASF Nederland B.V. (Masterheobuild) with 40% effective solid content. Purified silica sand (specific gravity 2650 kg/m^3, maximum particle size 2 mm, fineness modulus 2.05) was applied as the aggregate to prepare the AAM mortars, which was provided by Vandevelde N.V. The cumulative percentage passing curve of silica sand measured with sieving analysis is shown in Fig. 3, and the composition of silica sand determined by XRF test is presented in Table 1.

3.2. *Mix design of two-stream AAMs*

Details of mixture proportions in each individual stream are shown in Table 3 (expressed as in total per 100 g of solid precursor). For the purpose to meet various setting demands in different practical scenarios, the composition of stream A was varied while stream B was kept constant to achieve the different mixtures investigated in this study. Starting from A1, stream A is designed to introduce the primary precursor (BFS) into the AAMs. PNS is applied with a dosage of 0.5% by mass of solid precursors to reduce the water demand in stream A, which has been proven with no significant retarding effects on the subsequent activation reaction [48]. In the meantime, stream B plays the role to bring in concentrated alkaline activators with the secondary aluminosilicate source (EFS). Alkaline activators were prepared by dissolving sodium hydroxide and sodium silicate in tap water 24 h before mixing. However, the silicate activators may provide a dispersing effect at early ages to reduce the yield stress in AAM mixtures [45,49], which is unfavorable in view of 3D-printing applications (section 4.4). Thereby, PC was blended into stream A (up to 30%) to partially replace the BFS in A2, A3, and A4, aiming to accelerate the early structural build-up in AAMs [50,51] after combining individual streams.

An overview of the two-stream AAM mixture proportions is illustrated in Table 4. The water to binder (w/b) ratio is fixed at 0.35 in both streams (Note: binder refers to the sum of precursors and solid activators). Streams A and B are designed with a volume ratio of 1:1 for validation (section 4.4).

3.3. *Testing program*

3.3.1. *Investigation on paste levels*

The reaction kinetics and reaction products were investigated on paste fractions, as shown in Tables 3 and 4 by avoiding the sand fractions. Pastes of individual streams (Table 3) were prepared with a Hobart planetary mixer. The solid precursors were first dry-blended for 60 s. Subsequently, the activator was gradually added in 10 s, and the fresh paste was mixed at low speed (140 ± 5 rpm) and high speed (285 ± 5 rpm) for 90 s, respectively. To prepare the combined two-stream AAM pastes (Table 4), ready-mixed stream A and stream B mixtures were blended in the Hobart mixer with the low-speed mode for 10 s to simulate the intermixing process with the helical static mixer [52].

The exothermic behavior along the reaction progress was detected with a TAMAIR isothermal calorimeter. For each test, about 14 ± 0.01 g fresh paste was immediately transferred into a glass ampoule after mixing, then sealed and loaded into the isothermal channels of the calorimeter. Quartz sand with a specific heat flow of 0.71 J/(g.K) was applied as an inert reference. The heat flow was recorded as the difference between the sample and reference [53]. Results present in this study are normalized into 1 g of solid binder (including precursor and

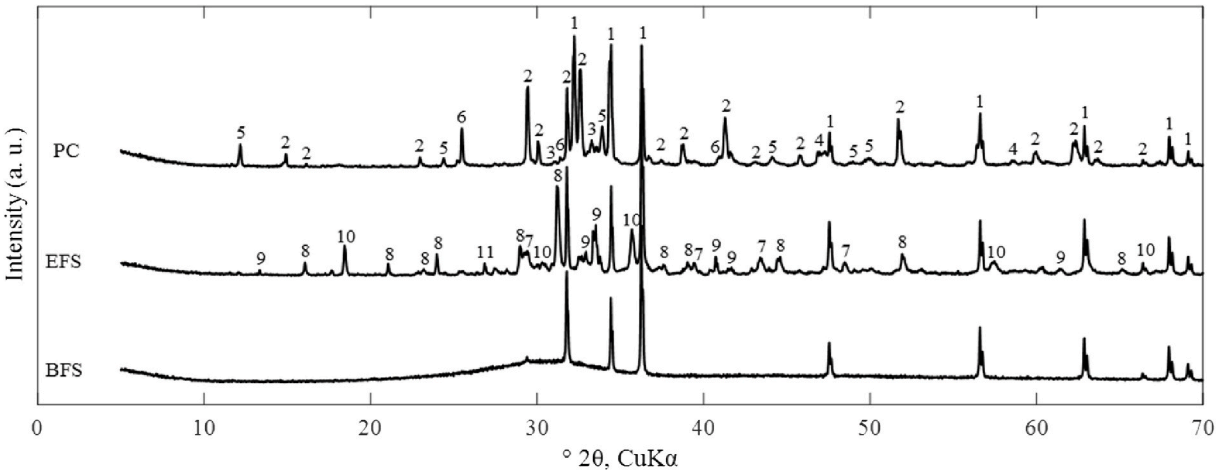

Fig. 4. XRD patterns of raw materials used in this study (1-Zincite (ZnO); 2-Alite (C_3S); 3-Belite (C_2S); 4-Aluminate (C_3A); 5-Ferrite (C_4AF); 6-Anhydrite ($CaSO_4$); 7-Calcite ($CaCO_3$); 8-Åkermanite ($Ca_2Mg(Si_2O_7)$; 9-Merwinite ($Ca_3Mg(SiO4)_2$); 10-Chromite ($FeCr_2O_4$); 11-Wollastonite ($CaSiO_3$)).

Table 2
Quantitative XRD analysis on the original mineral phases in raw materials.

	PC	EFS
Alite	55.4	0.0
Belite	13.2	0.0
Aluminate	5.5	0.0
Ferrite	16.1	0.0
Anhydrite	2.7	0.0
Calcite	0.5	8.9
Åkermanite	0.0	34.6
Merwinite	0.0	25.3
Chromite	0.0	12.0
Wollastonite	0.0	7.1
Amorphous and poorly crystalline phases	6.6	12.1

solid activators). Due to the thermal disturbance while inserting the glass ampoule, the heat recorded at the first 30 min was not compared among different samples. Calorimetry tests were performed twice in this study to check the repeatability of results.

Combined AAM pastes (Table 4) were cast into molds and sealed with plastic foils for further tests, and the samples were placed in a curing chamber (20 ± 0.5 °C, 95% relative humidity) until the testing age. The reaction products in combined AAMs were characterized at 30 min and 28 days after intermixing to interpret the early-stiffening process and the strength development by using different mixture proportions. In specific, the activation reaction was arrested by using a solvent replacement treatment with water and isopropanol [14]. Solid fractions collected from filtration were vacuum-dried and ground to pass a 63 μm sieve for characterization, and 10% (by mass) of zincite was intermixed as an internal standard [54]. Samples were stored in a sealed bottle inside a vacuum chamber until testing. XRD tests were conducted using a Bruker D8 Advance diffractometer with Cu-Kα radiation (λ = 1.54 Å) to characterize the mineralogical phases formed in the reaction products. For each sample, XRD tests were performed twice to check the repeatability. XRD patterns were recorded at the range between 10° and 70° with a step size of 0.02°. The Rietveld refinement was performed

Table 3
Mix design of AAMs in individual streams.

Mix	Precursor (g)			Activator solution (g)			PNS (g)[a]	Sand (g)	w/b[b]
	BFS	PC	EFS	NaOH	Sodium silicate solution	Extra water			
A1	50	0	0	–	–	17.13	0.625	60	0.35
A2	40	10	0	–	–	17.13	0.625	60	0.35
A3	30	20	0	–	–	17.13	0.625	60	0.35
A4	20	30	0	–	–	17.13	0.625	60	0.35
B	0	0	50	2.58	13.33	13.17	–	60	0.35

[a] Solid content is 0.5% by the mass of precursor.

[b] Water to binder mass ratio, defined as the total water content in sodium silicate solutions, PNS, and extra water divided by the mass of solid binders (including precursor and solid activators).

Table 4
Mix design of combined two-stream AAMs – overview.

Mix	Precursor (g)				Activator solution					PNS (g)[c]	w/b[d]	Sand (g)
	BFS	EFS	PC	Total	NaOH (g)	Sodium silicate solution (g)	Water (g)	Na_2O content[a]	Ms[b]			
M1 (A1+B)	50	50	0	100	2.58	13.33	30.30	4%	1	0.625	0.35	120
M2 (A2+B)	40	50	10	100	2.58	13.33	30.30	4%	1	0.625	0.35	120
M3 (A3+B)	30	50	20	100	2.58	13.33	30.30	4%	1	0.625	0.35	120
M4 (A4+B)	20	50	30	100	2.58	13.33	30.30	4%	1	0.625	0.35	120

[a] Defined as the equivalent Na_2O content in alkaline activators by the mass of precursors.

[b] Defined as the molar ratio between SiO_2 and Na_2O in alkaline activators.

[c] Solid content is 0.5% by the mass of precursor in stream A.

[d] Binder is defined as the sum of solid precursors and activators.

with Topas software to quantitatively assess the crystalline phases [55, 56].

3.3.2. Investigation on mortar levels

The fresh and hardened properties of individual streams and the combined mixture were investigated on mortar level. Mortars of individual streams were prepared with a Hobart planetary mixer by following the same protocol indicated in section 3.3.1 including the sand fractions. Solid precursors and aggregates were dry-blended for 60 s before introducing the liquid component.

The rheology of individual streams was assessed by flow curve tests, and the results present were taken as the average of two measurements. Rheological tests were conducted with an Anton Paar 102 rheometer fitted with a 4-blade vane (radius of 15 mm and height of 40 mm). For each measurement, the fresh mortar was loaded into a cylindrical cup (radius of 35 mm and height of 100 mm, with inner ribs of 0.85 mm thickness to prevent slippage). The rheometer vane was then inserted into the fresh mortar. Flow curve tests were performed with the protocol illustrated in Fig. 5. Fresh mortars were first subjected to a pre-shear of 50 rpm for 30 s to reach the reference state and left at rest for 30 s. Subsequently, a stepwise increasing and decreasing shear was applied, ranging between 10 and 50 rpm. Each step lasted for 30 s, and the average torque of the last 10 s was collected to calculate the equilibrium-state response. It was also confirmed by reaching the equilibrium-state shear stress for each shear rate increment with a number of trial experiments before the protocol was set. Given the large gap between the vane edge and the rheometer cup (radius of vane/radius of cup was close to 0.7), descending parts of the flow curves after applying the plug flow correction were fitted with the Bingham model to determine the dynamic rheological parameters [57,58].

The workability retention in individual streams was characterized by the flow table test (according to ASTM C1437) over time. The flow table test was repeated every 30 min in the first 2 h, and a 1-min remixing was performed on the mortar prior to each measurement [59]. The results present were derived from the average of two measurements.

Mortars of individual streams were then intermixed with each other to check the early structural build-up and hardened properties. In specific, ready-mixed stream A and stream B mixtures were blended in a Hobart planetary mixer with the low-speed mode for 10 s to simulate the mixing process with the helical static mixer [52].

The combined mixture was then immediately loaded into a 100 mm^3 cubic mold for the slow penetration test, and the fresh sample was vibrated for 30 s to remove the air bubbles. Slow penetration tests were performed with a W + B universal testing machine, where the 3 kN loading cell was applied and fitted with a steel spherical penetration front (diameter of 15 mm) [60]. A loading rate of 0.5 mm/min was applied with a maximum displacement of 25 mm, and the measurement was recorded when the penetration front was half emerged in the fresh mortar until 30 min after intermixing. The force against penetration was converted into the yield stress developed in the material according to Eq. (1) [61]. For each sample, the slow penetration test was performed twice to check the repeatability.

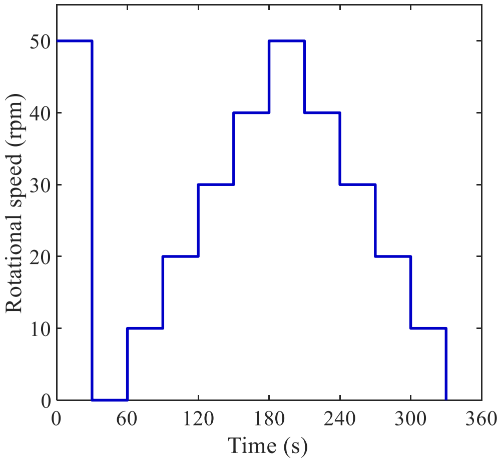

Fig. 5. Shear protocol for flow curve tests in this study.

$$\tau_0(t) = \frac{F(t)}{3\pi R^2} \tag{1}$$

where: $\tau_0(t)$ is the yield stress (Pa), $F(t)$ is the force against penetration (N), and R is the radius of the spherical penetration front (m).

The compressive strength of hardened mortars was tested at 1, 7, and 28 days according to EN196-1. Immediately after intermixing streams A and B, the combined mortars were cast into $40 \times 40 \times 160$ mm^3 molds and vibrated for 30 s to compact and eliminate the entrapped air bubbles. Mortars were then covered with a plastic sheet and transferred into a curing chamber (20 ± 0.5 °C with 95% relative humidity). Hardened mortar prisms were demolded after 24 h and sealed with plastic foils, the specimens were placed in the curing chamber until the testing age.

Finally, SEM and mercury intrusion porosimetry (MIP) tests were performed on hardened mortars taken from the combined mixtures to investigate the microstructure and elaborate the strength development. Hardened mortars, at the age of 28 days, were split into small pieces and immersed in isopropanol to stop the activation reaction. The samples were then filtered (with a 0.45 μm filter paper), and the filtered residue was vacuum dried (in an oven at 40 °C for about 5 min) to remove the remaining isopropanol [52]. Mortar samples were epoxy impregnated, and subjected to grinding and polishing to obtain a smooth surface, which was then coated with a thin layer of carbon before SEM tests (with JEOL JSM-7400F) [29]. The backscattered electron (BSE) mode was applied to visualize the microstructure developed in hardened specimens, accompanied by Energy Dispersive X-ray (EDX) spectroscopy analysis on the BSE images. MIP tests were conducted with a mercury intrusion porosimeter (ThermoFischer Scientific Pascal 140 & 440 series) to study the pore structure, with a maximum pressure of 200 MPa. The contact angle between the mercury and the specimen surface and the surface tension were set as 140° and 0.48 N/m, respectively [62]. For each mixture, the MIP test was performed on three replicate samples to ensure repeatability, and the curve most close to the average of three measurements is presented.

3.3.3. Validation

The conceptual design of two-stream AAMs was validated for different practical scenarios with the twin-pipe pumping system [46]. By using two progressive cavity pumps, ready-mixed individual mixtures A and B were simultaneously transported to the nozzle. A helical static mixer with 18 mixing elements was positioned before the end of the nozzle, and the individual stream mixtures were intermixed while passing through the static mixer.

The two-stream AAM system was first validated for self-compacting concrete applications. After extrusion from the twin-pipe nozzle, the combined AAM mixture was loaded into a V-Funnel to assess the filling ability and segregation resistance [63]. The discharging time was measured according to EN 12350-9 and expressed as the average of three measurements.

As aforementioned that various setting demands can be met by varying the mix design, the feasibility of applying two-stream AAMs in concrete 3D printing was also validated. The printing was carried out using an industrial robot (ABB IRB6650) with six degrees of freedom. The industrial robot has a payload capacity of 125 kg, capable of operating within a 3.2 m range, and move in any orientation and tool alignment [64,65]. A square column of 600 mm side length was printed using a 25 mm diameter circular nozzle. The horizontal and vertical printing speed were set as 200 mm/s and 2.22 mm/s, respectively [52]. The printing was continued until a column height of 1 m was achieved.

The printed column had a layer width of 25 mm and layer height of 10 mm.

4. Results and discussion

4.1. Properties of individual streams

4.1.1. Reaction kinetics

The normalized heat flow curves of individual streams are presented in Fig. 6. No apparent heat release was observed in A1 and B up to 48 h after the initial dissolution peak, indicating a very limited reaction progress if they are not intermixed. By substituting BFS with PC, the acceleration peak was observed A2. The acceleration peak gradually became broader in A3 and A4, which is ascribed to the intensified hydration of PC with a higher PC content in the system. It is noteworthy that among all mixtures the heat flow after the initial dissolution peak remained at a relatively low level close to zero at the beginning of 5 h (enlarged view in Fig. 6). The most intensive acceleration peak was detected in A4 with 30% PC, and was initiated after around 6 h. Results further illustrated a limited reaction rate at this stage. It is indicated that the fresh properties in individual streams could be maintained for a long term by using two-stream AAMs from the chemical reaction point of view.

4.1.2. Rheology and workability retention

Descending flow curves after applying plug flow corrections are plotted in Fig. 7 (a), and it was found that the slope gradually declined accompanied by a higher intercept with an increased PC content. Dynamic rheological parameters of individual streams by fitting the Bingham model are summarized in Table 5. The maximum yield stress was detected in A4 with the highest PC content. An increase in BFS content has led to lower yield stress and higher viscosity in the dispersing system prepared with water, which is in line with the knowledge in PC mixtures [66]. Meanwhile, stream B exhibited lower yield stress and a similar level of viscosity compared to stream A mixtures. Results of flow table tests in the first 2 h are shown in Fig. 7 (b). The maximum flow diameter was detected in A1, and slightly declined with a higher PC content. It is noteworthy that all mixtures showed a very limited loss in flow diameter after 2 h, which is in agreement with the calorimetry results, indicating good workability retention in individual streams.

4.2. Properties of combined two-stream AAMs

4.2.1. Reaction kinetics

The normalized heat flow in combined mixtures after intermixing is presented in Fig. 8. A long induction period was observed in M1, and the onset of the acceleration-stage reaction was detected after 24 h, which is in parallel with previous findings [67,68]. As shown in Fig. 8, the acceleration-stage reaction was significantly advanced with the increase in PC substitution level, accompanied by a more narrow and intensive acceleration peak. In M4 (with 30% PC), the dissolution and acceleration peaks partially overlapped with each other, and the maximum heat flow of 1.55 mW/g occurred at 1.2 h, which reveals a very vigorous early reaction progress in M4.

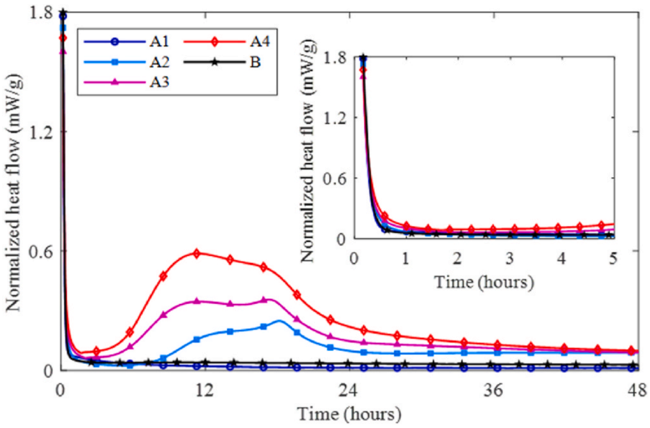

Fig. 6. Normalized heat flow as a function of time in individual streams.

4.2.2. Early age structural build-up

Results of slow penetration tests are presented in Fig. 9 to reveal the yield stress evolution in combined mixtures. No apparent build-up was detected in M1, and it was found that the yield stress maintained close to 0 MPa until the end of the measurement. Instead, the early build-up in combined mixtures was significantly accelerated with an increased PC content. By applying 30% PC, approximately 2.5 MPa yield stress has been developed in M4 after 30 min, which is in parallel with the intensive early exothermic reactions as shown in Fig. 8. The results have illustrated an adequate structuration rate for 3D-printing applications with respect to those reported in previous studies [60,69].

4.2.3. Early reaction products

The XRD patterns of two-stream AAMs at 30 min are presented in Fig. 10. Crystalline phases originating from EFS (Åkermanite, Merwinite, Chromite, and Wollastonite) have been identified in all samples. In addition, anhydrous phases from PC (Alite, Belite, Aluminate, and Ferrite) were detected in M2, M3, and M4. Moreover, diffuse humps located at around 29°, 33°, and 50° 2θ were ascribed to the formation of C-(A)-S-H phases at early stages through the activation reaction [70,71]. Further, quantitative analysis was conducted with the Rietveld method by using 10% zincite as an internal standard, and the results are shown in Table 6. It was found that the anhydrous phases from PC gradually increased with a higher PC content in the system, accompanied by a slight reduction in the crystalline phases that originated from EFS. In addition, a trace amount of Portlandite, as a typical reaction product from PC hydration, has been detected in M2, M3, and M4. It is noteworthy that other types of PC hydration products were not detected in the system at 30 min, which suggests the majority of PC was dissolved by the activator to contribute to the formation of C-(A)-S-H phases. Due to the amorphous nature of the BFS precursor and C-(A)-S-H reaction products, it was challenging to understand the phase transition by quantitative XRD analysis on these phases. Instead, the mass of PC and EFS were calculated with Eq. (2). As illustrated in Table 6, a considerable fraction of PC has been dissolved in the two-stream AAMs up to 30 min, contributing to the accumulation of early reaction products, which in turn resulted in the stiffness development during the early structuration. Meanwhile, only a limited portion of EFS has been dissolved during the same period, which reveals the lower reactivity of EFS compared to PC. The results further illustrate that a higher PC content has promoted the dissolution of EFS in the system, given a constant EFS content among all mixtures.

$$M_d = \frac{m_1 - m_2}{m_1} \times M_0 \tag{2}$$

where m_1 (g) is the mass of raw materials (PC or EFS) in the XRD sample, m_2 (g) is the mass of remaining anhydrous phases from PC or EFS in the XRD sample at 30 min.

4.3. Hardened properties

4.3.1. Compressive strength development

The 1-, 7-, and 28-day compressive strength of hardened samples are shown in Fig. 11. It was found in general that the higher the PC content the lower the strength developed in the hardened mortar. After 28 days, the compressive strength of M1 reached 45 MPa, whereas a 10%

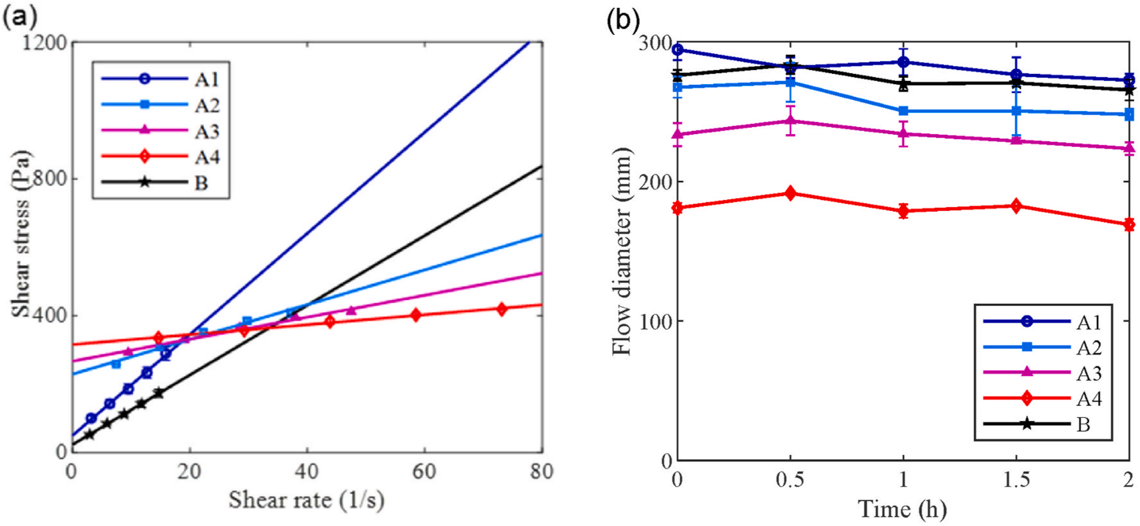

Fig. 7. Fresh properties of mixtures in individual streams (a) Flow curves; (b) Flow diameters as a function of time (Results were taken as the average of two measurements, the error bar represents the standard deviation).

Table 5
Dynamic rheological parameters of fresh mortars in individual streams.

	A1	A2	A3	A4	B
Dynamic yield stress (Pa)	49.6	228.9	266.8	315.3	23.1
Plastic viscosity (Pa·s)	14.8	5.1	3.2	1.5	10.2

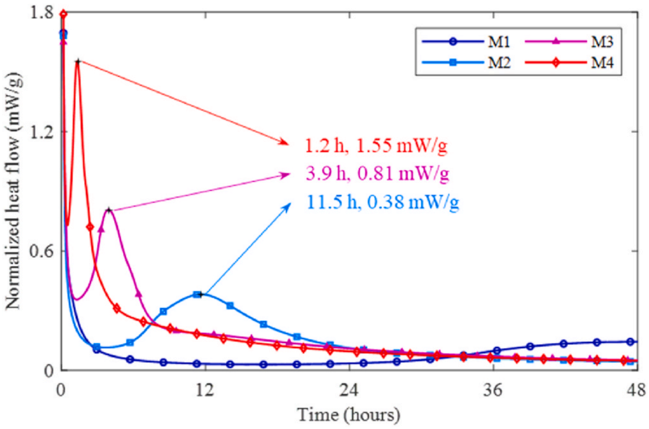

Fig. 8. Normalized heat flow as a function of time in combined two-stream AAMs.

replacement of BFS with PC led to a 13% strength reduction in M2. Moreover, it is noteworthy that M1 exhibited the lowest 1-day compressive strength as compared to those mixtures with PC involved. This is attributed to the reaction kinetics as presented in Fig. 8. M1 was still entrapped in the long induction stage to obstruct the early strength development [67,72,73], whereas the acceleration peaks have almost ended in the other mixtures up to 24 h.

4.3.2. Long-term reaction products

XRD patterns of two-stream AAM samples at 28 days are shown in Fig. 12, and the results of quantitative XRD analysis are presented in Table 7. As the reaction progressed, it was found that the content of undissolved crystalline phases from EFS and anhydrous phases from PC further declined in all mixtures. In the meantime, the amorphous content gradually increased, indicating the accumulation of amorphous reaction products. This is accompanied by a slight increase in Portlandite content in the 28-day samples. In addition, monocarboaluminate and hydrotalcite phases have been identified as new types of reaction products in the system after 28 days. Monocarboaluminate is recognized as a typical reaction product from PC hydration [74], and higher monocarboaluminate content has been detected in the mixtures with an increase in PC content at 28 days. The hydrotalcite content declined with a reduction of BFS ratio in the system, as it is known as a major long-term reaction product in silicate-activated slag mixtures [70,72]. Compared to the results presented in Tables 6, it was found that the majority of the dissolution of PC took place at the first 30 min to contribute to the early structuration, while the amorphous C-(A)-S-H phases were characterized as the major reaction product in the system at this stage. Instead, only a limited portion of PC was further dissolved between 30 min and 28 days to assist in the strength development, accompanied by the accumulation of C-(A)-S-H, portlandite, monocarboaluminate, and hydrotalcite reaction products. Moreover, EFS content progressively dissolved between 30 min and 28 days, while its dissolution rate is much lower compared to that of PC.

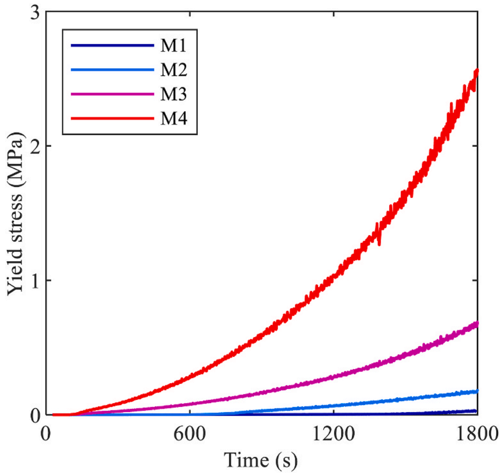

Fig. 9. Yield stress as a function of time in combined mixtures defined by slow penetration test.

4.3.3. Microstructure of hardened samples

The microstructure of 28-day two-stream AAM mortars was

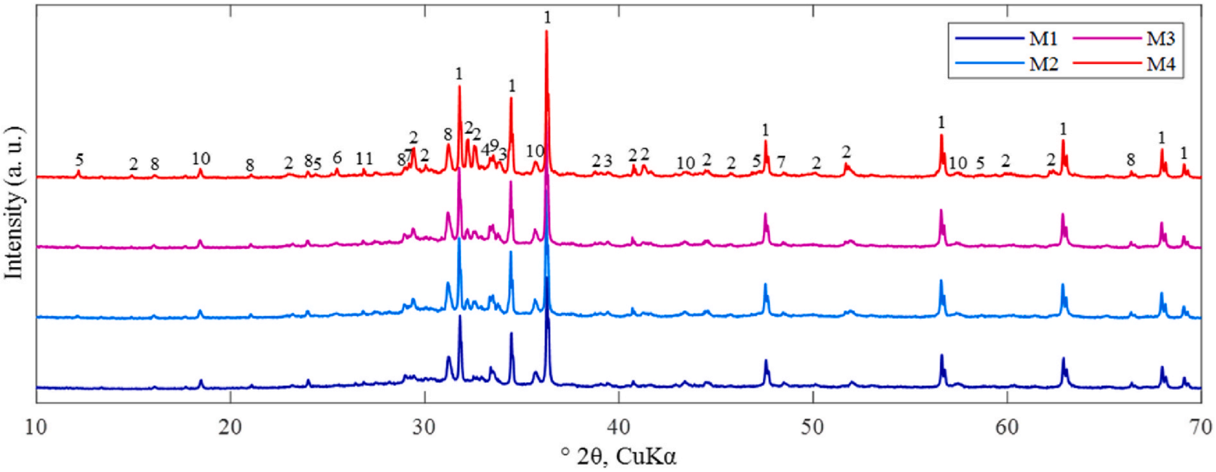

Fig. 10. XRD patterns of two-stream AAMs at 30 min (1-Zincite (ZnO); 2-Alite (C_3S); 3-Belite (C_2S); 4-Aluminate (C_3A); 5-Ferrite (C_4AF); 6-Anhydrite ($CaSO_4$); 7-Calcite ($CaCO_3$); 8-Åkermanite ($Ca_2Mg(Si_2O_7)$; 9-Merwinite ($Ca_3Mg(SiO4)_2$); 10-Chromite ($FeCr_2O_4$); 11-Wollastonite ($CaSiO_3$)).

Table 6
Quantitative XRD analysis on the phases formed in two-stream AAMs at 30 min.

	M1	M2	M3	M4
Alite	0.0	4.1	9.3	11.6
Belite	0.0	4.6	4.9	5.6
Aluminate	0.0	2.2	1.6	1.7
Ferrite	0.0	1.9	2.8	3.9
Anhydrite	0.0	0.0	0.0	0.0
Calcite	3.6	4.3	4.5	2.8
Åkermanite	14.6	13.7	14.0	10.0
Merwinite	10.5	7.0	7.9	5.6
Chromite	3.7	3.5	4.1	3.2
Wollastonite	5.8	5.4	4.7	3.1
Portlandite	0.0	0.8	0.3	1.1
Amorphous and poorly crystalline phases	61.75	52.47	45.83	51.44
PC dissolved/PC added (g/g)	0/0	8.28/10	15.36/20	22.31/30
EFS dissolved/EFS added (g/g)	11.8/50	14.1/50	16.8/50	25.3/50

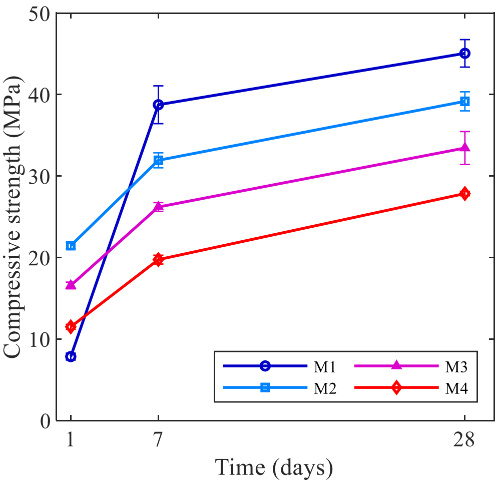

Fig. 11. Compressive strength of combined two-stream AAM mortars (Results were taken as the average strength of three specimens, the error bar represents the standard deviation).

visualized through SEM analysis. As presented in Fig. 13, different phases could be identified in the BSE images. The coarse particles in dark grey colors represent the aggregates, whereas the smaller light grey grains refer to the undissolved Ca-rich precursors. The voids between solid particles are filled with reaction products, and the black regions indicate the microcracks and pores formed in the hardened samples. It was observed that some of the precursor grains retained the angular morphology and were somewhat detached from the matrix (solid rectangular in Fig. 13 (b)), which might be ascribed to the less reactive EFS precursors. On the other hand, some precursor particles were tightly embedded in the hardened matrix and surrounded by a dense layer of reaction rim (dashed rectangular in Fig. 13 (b)), referring to the more reactive PC and BFS particles. Moreover, significant microcracks were observed in Fig. 13 (a) between solid grains, which might be attributed to the high amount of drying shrinkage of gel reaction products reported in silicate-activated slag systems [75,76]. It is noteworthy that the microcracks in the matrix were considerably mitigated with the increase in PC content (Fig. 13 (c) and (d)), which is possibly correlated to the variation in the reaction products (Table 7).

The chemical composition of interparticle reaction products was then studied on interparticle matrix regions, and 15 random spots were selected to perform the EDX analysis. Previous studies have revealed that the elemental concentration could be affected by the dissolution in the region adjacent to the precursor grains [76,77]. Thereby, the spots selected were located at least 5 μm from the surface of the solid grains. Results of the average atomic ratio obtained by EDX analyses are summarized in Table 8. The highest Ca/Si ratio of 1.46 was detected in M4, and the Ca/Si ratio gradually declined with a higher BFS content in the system. It was noticed that a higher Ca/Si ratio in the reaction products is associated with the strength reduction of hardened samples, which is possibly attributed to the higher surface area and lower molar volume of the C–S–H phases due to a decreased Ca/Si ratio [78]. Meanwhile, a higher PC content also led to the increase in Al/Si and Na/Si ratios as shown in Table 8. The increase in Al/Si ratio in reaction products could be correlated to the presence of more Al-containing crystalline phases as shown in Table 7, as well as a higher degree of Al-uptake in Si tetrahedron structures Moreover, the Mg/Al ratio in the reaction products of M2 (with 10% PC) was about 50% higher compared to that detected in the reference mixture M1, which further increased in M3 and M4 with a higher PC content. Mg typically presents in hydrotalcite phases in an AAM system, with a characteristic Mg/Al ratio of approximately 2. [72,79,80], which is much higher than the results shown in Table 8. Regarding the phases identified in the current system (Table 7), it is possible that the Mg content might be optionally incorporated into the amorphous binding chains in C-(A)-S-H phases [81] or contributed to the formation of magnesium-silicate-hydrate (M-S-H) phases [82,83]. Besides, hydrotalcite with much lower Mg/Al has also been reported [84], depending on the availability of Al sources in the raw material

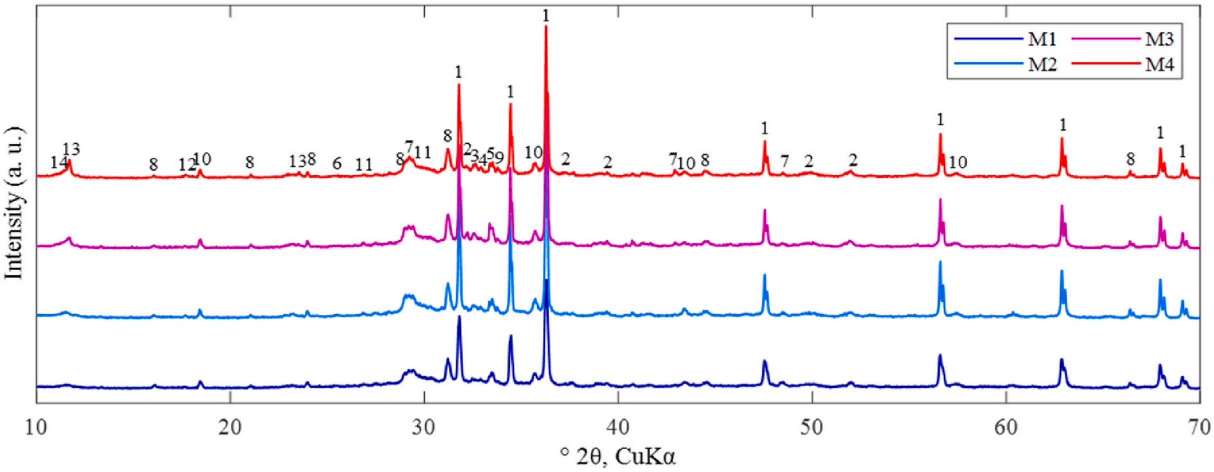

Fig. 12. XRD patterns of two-stream AAMs at 28 days (1-Zincite (ZnO); 2-Alite (C_3S); 3-Belite (C_2S); 4-Aluminate (C_3A); 5-Ferrite (C_4AF); 6-Anhydrite ($CaSO_4$); 7-Calcite ($CaCO_3$); 8-Åkermanite ($Ca_2Mg(Si_2O_7)$); 9-Merwinite ($Ca_3Mg(SiO4)_2$); 10-Chromite ($FeCr_2O_4$); 11-Wollastonite ($CaSiO_3$); 12-Portlandite ($Ca(OH)_2$); 13-Monocarboaluminate ($CH_{22}Al_2Ca_4O_{20}$); 14-Hydrotalcite ($Mg_6Al_2CO_3(OH)_{16}{\cdot}4H_2O$)).

Table 7
Quantitative XRD analysis on the phases formed in two-stream AAMs at 28 days.

	M1	M2	M3	M4
Alite	0.0	1.3	2.8	2.4
Belite	0.0	1.9	4.3	3.3
Aluminate	0.0	0.8	2.3	1.1
Ferrite	0.0	1.5	1.7	0.5
Anhydrite	0.0	0.0	0.0	0.0
Calcite	6.0	5.3	6.0	5.9
Åkermanite	12.0	9.9	11.1	10.1
Merwinite	6.7	1.7	3.0	2.1
Chromite	3.0	2.4	2.1	0.8
Wollastonite	4.9	4.3	5.0	4.8
Portlandite	0.0	0.8	1.7	1.9
Monocarboaluminate	0.0	1.1	3.4	6.0
Hydrotalcite	1.0	0.1	0.2	0.2
Amorphous and poorly crystalline phases	66.4	69.0	56.2	60.9
PC dissolved/PC added (g/g)	0/0	8.92/10	16.56/20	26.02/30
EFS dissolved/EFS added (g/g)	17.4/50	19.4/50	22.8/50	26.3/50

[85]. Nevertheless, the EDX beam size should also be considered, which might be significantly larger compared to the Mg- and Al-containing phases formed in the matrix at different spots for EDX analyses [86].

It is known that ionic species dissolved from precursors play different roles in the synthesis of reaction products in AAMs [42]. Al and Si species are interconnected with each other through polymerization to assemble the backbone structure, while the alkali and alkali-earth cations are further incorporated to balance the negative charging sites of Al and Si tetrahedrons [10,87,88]. The atomic (2Ca+2Mg+K+Na)/Si ratio was plotted against the Al/Si ratio as presented in Fig. 14. In general, the reaction products in M1 exhibited better homogeneity in composition, with the (2Ca+2Mg+K+Na)/Si ratio ranging from 2.5 to 3, and the Al/Si ratio ranging between 0.2 and 0.4. As suggested by previous researchers [76,89], from the composition point of view, the reaction products of M1 are assigned to C-(N)-A-S-H types of gels formed in AAMs (as indicated by the dashed circle in Fig. 14). In contrast, the chemical composition of reaction products in M4 is apparently more scattered, which can be correlated to the various complex phases formed in the system as indicated by the XRD result (Table 7).

Further, it can be seen that the (2Ca+2Mg+K+Na)/Si ratio in reaction products gradually increased with a higher PC content. The results indicate that the inclusion of PC has promoted the dissolution of multiple cations and their incorporation in the reaction products. On the other hand, the Al/Si ratio further deviated from the average value while a higher PC content is included in the system. Regarding the raw material compositions (Table 1), the substitution of BFS with PC has resulted in a declined availability of Al source in the system. However, several spots in M2, M3, and M4 were detected with a significantly higher Al/Si ratio as compared to those of M1. This can be ascribed to the rapid stiffening process as revealed by the slow penetration test (Fig. 9). By using high-modulus silicate activators in AAMs, the release of silicate species from precursors is more delayed compared to Al species as well as other cations [90,91], referring to the long induction-stage reactions. As a consequence of the rapid setting of the mixture, a dense layer of reaction products could be expected to form on the outer surface of precursors (especially the grains with higher reactivity), obstructing subsequent ion diffusion into the matrix at later ages [76]. Thereby, Si species with reduced availability are less incorporated into the reaction products in some regions of the matrix (depending on the reactivity of adjacent precursor grains), locally resulting in a higher Al/Si ratio in the matrix.

The pore structure developed in 28-day mortars were then assessed with MIP. As shown in Fig. 15 (a), the pores detected could be categorized into (1) small gel pores (below 10 nm), (2) large gel pores (10–100 nm), and (3) capillary pores (around 1 μm) depending on the pore size [76]. More small gel pores were detected in M1, and the amount of small gel pores was reduced with a higher content of PC in the system. Instead, the peak of large gel pores gradually broadened and shifted to the right when increasing the PC replacement level, indicating the formation of more larger gel pores in hardened samples. Meanwhile, the peak referring to the capillary pores located at around 1 μm also intensified with a higher PC content. The highest cumulative intruded volume was observed in M4 with 30% PC in the system, which was almost doubled as compared to M1. Results obtained for the pore structure are in line with the 28-day strength development. It is indicated that the substitution of BFS with PC may lead to a more porous microstructure in hardened samples, declining the mechanical strength. As mentioned in the previous paragraph, the rapid setting progress may result in fast precipitation of relatively dense layer of reaction products on the precursor surface to inhibit further ion exchange. This can be analogized to the dense C–S–H rims observed around the precursor grains in sodium hydroxide-activated slag mixtures [72]. Thereby, more vacancies and interparticle voids are formed in the matrix, leading to a porous microstructure (Fig. 15).

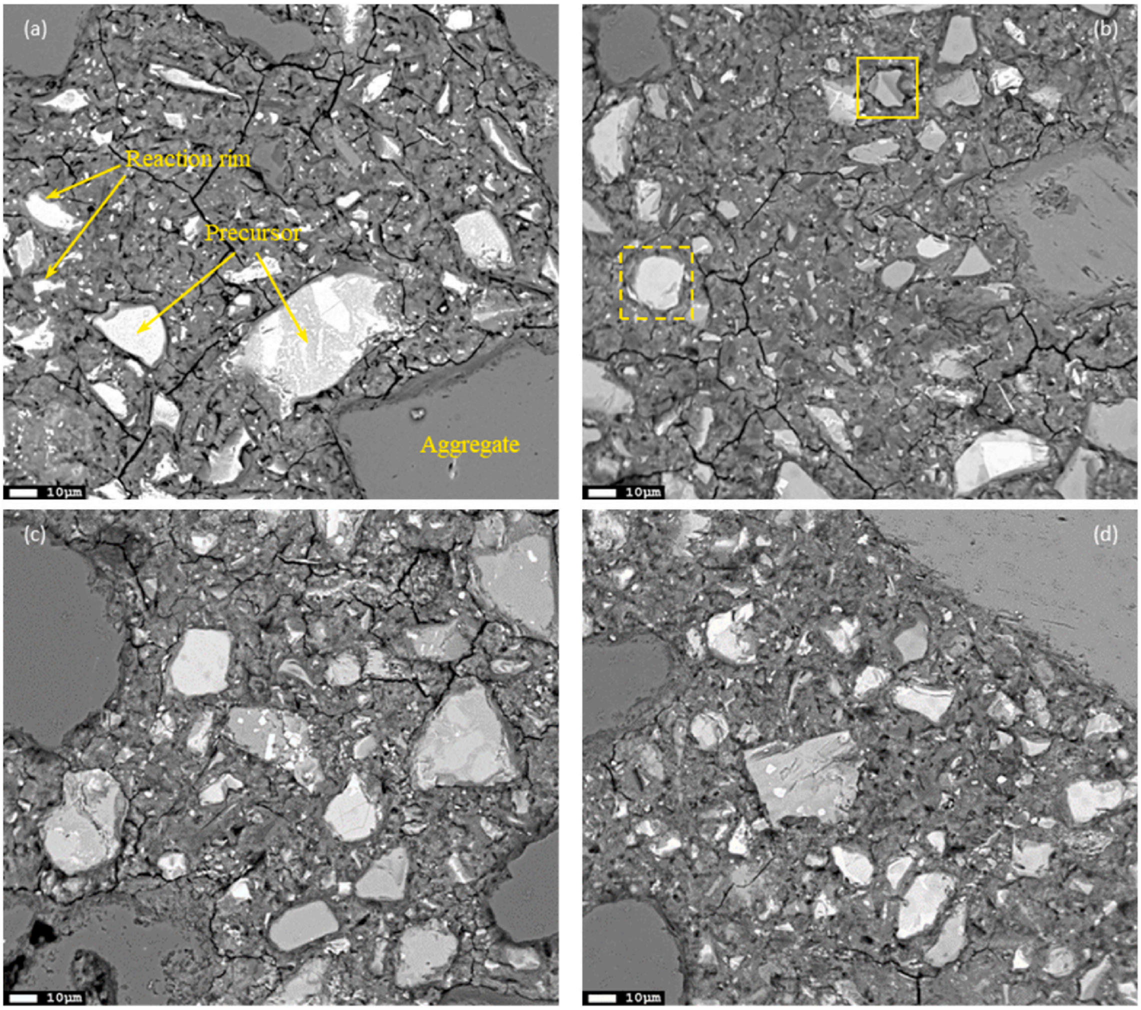

Fig. 13. BSE images of hardened two-stream AAM mortars at the age of 28 days (a) M1; (b) M2; (c) M3; (d) M4.

Table 8
Average atomic ratio obtained by EDX analyses at 28 days.

	Ca/Si	Al/Si	Na/Si	Mg/Al
M1	1.02 ± 0.10	0.23 ± 0.04	0.44 ± 0.12	0.41 ± 0.17
M2	1.12 ± 0.14	0.26 ± 0.09	0.63 ± 0.11	0.63 ± 0.20
M3	1.26 ± 0.18	0.27 ± 0.12	0.67 ± 0.27	0.69 ± 0.32
M4	1.46 ± 0.23	0.31 ± 0.10	1.07 ± 0.31	0.79 ± 0.44

4.4. Validation and perspectives

The concept of two-stream AAMs was validated with the twin-pipe pumping system. As shown in Fig. 16 (a), individual stream mixtures were prepared separately and further intermixed with the static mixer before casting. Mixture M1 (obtained after intermixing A1 and B) was first loaded into the V-Funnel (Fig. 16 (a)), and the result of discharging time is presented in Table 9. It is indicated that M1 could be regarded as a self-compacting mixture appropriate for high-fluidity applications. Moreover, mixture M4 (obtained after intermixing A4 and B) was then prepared for the 3D-printing application to construct the column structure (Fig. 16 (b)). The height of the column reached 1 m within 10 min, suggesting M4 is suitable for applications where a high build-up rate is demanded.

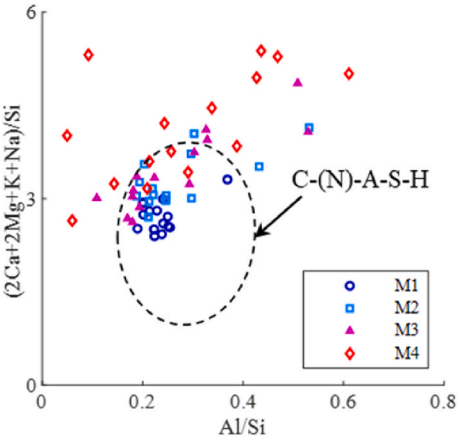

Fig. 14. Atomic (2Ca+2Mg+K+Na)/Si ratio against Al/Si ratio in the reaction products of two-stream AAMs at the age of 28 days.

The results presented in this study have illustrated that the concept of 'two-stream AAMs' could be adapted into the existing equipment developed for traditional PC concrete (mixers, pumps, etc.) by simple refitting. In specific, individual stream mixtures can be prepared and delivered to the construction site separately with parallel devices, and a final-stage intermixing is required before casting to trigger the major activation reaction. Two-stream AAMs may not only resolve the workability issues by using conventional SP and sodium silicate to disperse solid particles in individual mixtures, but also ensure sufficient open

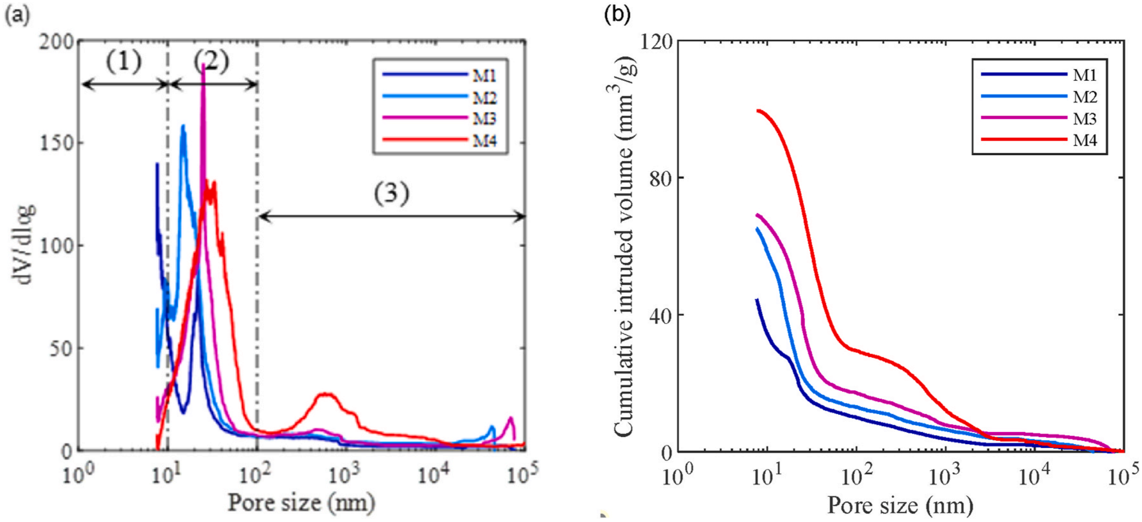

Fig. 15. Pore structure developed in 28-day mortars (a) Pore size distribution; (b) Cumulative pore volume.

Fig. 16. Validation of the two-stream AAM concept (a) Scenario 1: Self-compacting application (with M1); (b) Scenario 2: 3D-Printing application (with M4).

Table 9
V-Funnel discharging time of M1.

Test	1	2	3	Average
Discharging time (s)	9.9	10.1	9.3	9.8

time while delivering to the construction site in practical applications. From a future perspective, the mix design and volume ratio of separate streams could be further modified to meet the setting demand after casting and various engineering properties of hardened AAM concretes.

5. Conclusions

A conceptual design of two-stream alkali-activated materials (AAMs) has been proposed in the current study to resolve the rheological issues of AAMs. The solid and liquid components in AAMs are divided into separate fractions, where a very limited reactivity is expected in individual streams. By using the two-stream approach, a much longer workability retention has been achieved compared to conventional AAMs. The rheology of individual streams could also be modified by using conventional superplasticizers (SPs) and silicate activators, respectively. A final-stage intermixing between separate streams is required to trigger the major activation reaction. The combined two-stream mixtures were further validated in different practical scenarios including self-compacting and 3D-printing concrete applications.

Low yield stress and viscosity have been detected in individual streams for all mixtures. In addition, calorimetry results reveal that the exothermic reaction after the initial dissolution remained at a relatively low level for up to 5 h. The workability retention was also confirmed by the flow table test over time, where no significant loss in workability has been detected among all mixtures. The self-compacting application was validated by V-Funnel tests, with an average discharging time of 9.8 s.

Further, Portland cement (PC) was partially blended into the system to alter the early stiffening process to meet various setting demands. By replacing 30% blast furnace slag (BFS) with PC, the yield stress developed in the combined mixture reached 2.5 MPa after 30 min to achieve rapid structuration. However, an increased PC content on the other hand led to a reduced compressive strength in hardened samples at the age of 28 days, which is associated with the formation of more porous microstructures and the increase in the Ca/Si ratio in reaction products. Portlandite and monocarboaluminate have been identified in the reaction products in addition to the conventional C-(A)-S-H and hydrotalcite phases in typical silicate-activated slag mixtures. Eventually, the mixture with 30% PC was validated for 3D-printing applications, and a column of 1 m was constructed within 10 min.

CRediT authorship contribution statement

Yubo Sun: Writing – review & editing, Writing – original draft, Methodology, Investigation, Formal analysis, Data curation, Conceptualization. **Manu K. Mohan:** Writing – review & editing, Writing – original draft, Methodology, Investigation, Conceptualization. **Yaxin Tao:** Writing – review & editing, Writing – original draft, Methodology, Investigation. **Yi Zhang:** Writing – review & editing, Writing – original draft, Methodology, Investigation. **Kim Van Tittelboom:** Writing – review & editing, Supervision. **Guang Ye:** Writing – review & editing. **Geert De Schutter:** Writing – review & editing, Supervision, Funding acquisition.

Declaration of competing interest

The authors declared that we have no conflicts of interest in this work. We declare that we do not have any commercial or associative interest that represents a conflict of interest in connection with the work submitted.

Data availability

Data will be made available on request.

Acknowledgments

This paper presents the research results from the DuRSAAM project. The authors wish to acknowledge the financial support from the European Union's Horizon 2020 research and innovation programme (ETN DuRSAAM – H2020-MSCA-ITN-2018-813596).

References

[1] J.S.J. van Deventer, C.E. White, R.J. Myers, A roadmap for production of cement and concrete with low-CO2 emissions, Waste and Biomass Valorization 12 (2021) 4745–4775.

[2] M.C.G. Juenger, F. Winnefeld, J.L. Provis, J.H. Ideker, Advances in alternative cementitious binders, Cement Concr. Res. 41 (2011) 1232–1243, https://doi.org/10.1016/j.cemconres.2010.11.012.

[3] A. Sivakrishna, A. Adesina, P.O. Awoyera, K.R. Kumar, Green concrete: a review of recent developments, Mater. Today Proc. 27 (2020) 54–58, https://doi.org/10.1016/j.matpr.2019.08.202.

[4] P. Duxson, D.G. Brice, Chemical Research and Climate Change as Drivers in the Commercial Adoption of Alkali Activated Materials (2010) 145–155, https://doi.org/10.1007/s12649-010-9015-9.

[5] J.L. Provis, Geopolymers and other alkali activated materials: why, how, and what? Mater. Struct. Constr. 47 (2014) 11–25, https://doi.org/10.1617/s11527-013-0211-5.

[6] A. Fernández-Jiménez, J.G. Palomo, F. Puertas, Alkali-activated slag mortars: mechanical strength behaviour, Cement Concr. Res. 29 (1999) 1313–1321, https://doi.org/10.1016/S0008-8846(99)00154-4.

[7] M. Albitar, M.S.M. Ali, P. Visintin, M. Drechsler, Durability evaluation of geopolymer and conventional concretes, Construct. Build. Mater. 136 (2017) 374–385, https://doi.org/10.1016/j.conbuildmat.2017.01.056.

[8] T.A. Aiken, W. Sha, J. Kwasny, M.N. Soutsos, Cement and Concrete Research Resistance of geopolymer and Portland cement based systems to silage ef fl uent attack, Cement Concr. Res. 92 (2017) 56–65, https://doi.org/10.1016/j.cemconres.2016.11.015.

[9] S.A. Bernal, J.L. Provis, A. Fernández-jiménez, P. V Krivenko, E. Kavalerova, M. Palacios, C. Shi, Alkali Activated Materials, 2014. http://link.springer.com/10.1007/978-94-007-7672-2.

[10] P. Duxson, J.L. Provis, Designing precursors for geopolymer cements, J. Am. Ceram. Soc. 91 (2008) 3864–3869, https://doi.org/10.1111/j.1551-2916.2008.02787.x.

[11] M. Palacios, P.F.G. Banfill, F. Puertas, Rheology and setting of alkali-activated slag pastes and mortars: effect of organic admixture, ACI Mater. J. 105 (2008) 140.

[12] C. Qing-Hua, S.L. Sarkar, A study of rheological and mechanical properties of mixed alkali activated slag pastes, Adv. Cement Base Mater. 1 (1994) 178–184, https://doi.org/10.1016/1065-7355(94)90009-4.

[13] E. Douglas, A. Bilodeau, V.M. Malhotra, Properties and durability of alkali-activated slag concrete, Mater. J. 89 (1992) 509–516.

[14] M. Palacios, S. Gismera, M.M. Alonso, J.B. Espinose, D. Lacaillerie, B. Lothenbach, A. Favier, C. Brumaud, F. Puertas, Cement and Concrete Research Early reactivity of sodium silicate-activated slag pastes and its impact on rheological properties, Cement Concr. Res. 140 (2021) 106302, https://doi.org/10.1016/j.cemconres.2020.106302.

[15] M. Nodehi, V.M. Taghvaee, Alkali-activated materials and geopolymer: a review of common precursors and activators addressing circular economy, Circ. Econ. Sustain. 2 (2022) 165–196.

[16] A. Fernández-Jiménez, N. Cristelo, T. Miranda, Á. Palomo, Sustainable alkali activated materials: precursor and activator derived from industrial wastes, J. Clean. Prod. 162 (2017) 1200–1209.

[17] C.D. Atiş, C. Bilim, Ö. Çelik, O. Karahan, Influence of activator on the strength and drying shrinkage of alkali-activated slag mortar, Construct. Build. Mater. 23 (2009) 548–555.

[18] A. Fernández-Jiménez, F. Puertas, Setting of alkali-activated slag cement. Influence of activator nature, Adv. Cement Res. 13 (2001) 115–121.

[19] A.M. Rashad, Y. Bai, P.A.M. Basheer, N.B. Milestone, N.C. Collier, Hydration and properties of sodium sulfate activated slag, Cem. Concr. Compos. 37 (2013) 20–29, https://doi.org/10.1016/j.cemconcomp.2012.12.010.

[20] C. Lu, Z. Zhang, C. Shi, N. Li, D. Jiao, Q. Yuan, Rheology of alkali-activated materials: a review, Cem. Concr. Compos. 121 (2021) 104061, https://doi.org/10.1016/j.cemconcomp.2021.104061.

[21] M. Palacios, F. Puertas, Stability of superplasticizer and shrinkage-reducing admixtures Stability of superplasticizer and shrinkage-reducing admixtures in high basic media, Mater. Construcción 54 (2004) 65–86.

[22] J.-J. Chang, A study on the setting characteristics of sodium silicate-activated slag pastes, Cement Concr. Res. 33 (2003) 1005–1011.

[23] C. Sun, J. Sun, D. Wang, Effect of tartaric acid on the early hydration of NaOH-activated slag paste, J. Therm. Anal. Calorim. 144 (2021) 41–50.

[24] L. Xu, X. Wang, C. Guan, W. Wu, L. Zhang, The effect of activators on the mechanical properties and microstructure of alkali-activated nickel slag, Adv. Civ. Eng. 2020 (2020).

[25] S.Y. Oderji, B. Chen, C. Shakya, M.R. Ahmad, S.F.A. Shah, Influence of superplasticizers and retarders on the workability and strength of one-part alkali-activated fly ash/slag binders cured at room temperature, Construct. Build. Mater. 229 (2019) 116891, https://doi.org/10.1016/j.conbuildmat.2019.116891.

[26] N. Garg, C.E. White, Mechanism of zinc oxide retardation in alkali-activated materials: an in situ X-ray pair distribution function investigation, J. Mater. Chem. A 5 (2017) 11794–11804.

[27] X. Cong, W. Zhou, X. Geng, M. Elchalakani, Low field NMR relaxation as a probe to study the effect of activators and retarders on the alkali-activated GGBFS setting process, Cem. Concr. Compos. 104 (2019) 103399.

[28] D. Ravikumar, N. Neithalath, Effects of activator characteristics on the reaction product formation in slag binders activated using alkali silicate powder and NaOH, Cem. Concr. Compos. 34 (2012) 809–818, https://doi.org/10.1016/j.cemconcomp.2012.03.006.

[29] B.S. Gebregziabiher, R. Thomas, S. Peethamparan, Very early-age reaction kinetics and microstructural development in alkali-activated slag, Cem. Concr. Compos. 55 (2015) 91–102, https://doi.org/10.1016/j.cemconcomp.2014.09.001.

[30] M.C.G. Juenger, R. Snellings, S.A. Bernal, Supplementary cementitious materials: new sources, characterization, and performance insights, Cement Concr. Res. 122 (2019) 257–273.

[31] B. Das, S. Prakash, P.S.R. Reddy, V.N. Misra, An overview of utilization of slag and sludge from steel industries, Resour. Conserv. Recycl. 50 (2007) 40–57.

[32] M.F. Rojas, M.I.S. De Rojas, Chemical assessment of the electric arc furnace slag as construction material: expansive compounds, Cement Concr. Res. 34 (2004) 1881–1888.

[33] D. Kassim, G. Lamaa, R.V. Silva, J. de Brito, Performance enhancement of alkali-activated electric arc furnace slag mortars through an accelerated CO2 curing process, Appl. Sci. 12 (2022) 1662.

[34] Y. Jiang, T.-C. Ling, C. Shi, S.-Y. Pan, Characteristics of steel slags and their use in cement and concrete—a review, Resour. Conserv. Recycl. 136 (2018) 187–197.

[35] I. Sosa, C. Thomas, J.A. Polanco, J. Setién, J.A. Sainz-Aja, P. Tamayo, Durability of high-performance self-compacted concrete using electric arc furnace slag aggregate and cupola slag powder, Cem. Concr. Compos. 127 (2022) 104399.

[36] J.M. Manso, J.J. Gonzalez, J.A. Polanco, Electric arc furnace slag in concrete, J. Mater. Civ. Eng. 16 (2004) 639–645.

[37] F. Autelitano, F. Giuliani, Electric arc furnace slags in cement-treated materials for road construction: mechanical and durability properties, Construct. Build. Mater. 113 (2016) 280–289.

[38] J.-Y. Lee, J.-S. Choi, T.-F. Yuan, Y.-S. Yoon, D. Mitchell, Comparing properties of concrete containing electric arc furnace slag and granulated blast furnace slag, Materials 12 (2019) 1371.

[39] M. Češnovar, K. Traven, B. Horvat, V. Ducman, The potential of ladle slag and electric arc furnace slag use in synthesizing alkali activated materials; the influence of curing on mechanical properties, Materials 12 (2019) 1173.

[40] H. Hafez, D. Kassim, R. Kurda, R.V. Silva, J. de Brito, Assessing the sustainability potential of alkali-activated concrete from electric arc furnace slag using the ECO2 framework, Construct. Build. Mater. 281 (2021) 122559.

[41] N. You, B. Li, R. Cao, J. Shi, C. Chen, Y. Zhang, The influence of steel slag and ferronickel slag on the properties of alkali-activated slag mortar, Construct. Build. Mater. 227 (2019) 116614.

[42] J.L. Provis, J.S.J. Van Deventer, Alkali Activated Materials: State-Of-The-Art Report, Springer Science & Business Media, 2013. RILEM TC 224-AAM.

[43] M. Nodehi, T. Ozbakkaloglu, A. Gholampour, T. Mohammed, X. Shi, The effect of curing regimes on physico-mechanical, microstructural and durability properties of alkali-activated materials: a review, Construct. Build. Mater. 321 (2022) 126335.

[44] M.F. Alnahhal, T. Kim, A. Hajimohammadi, Distinctive rheological and temporal viscoelastic behaviour of alkali-activated fly ash/slag pastes: a comparative study with cement paste, Cement Concr. Res. 144 (2021) 106441, https://doi.org/10.1016/j.cemconres.2021.106441.

[45] Y. Sun, S. Zhang, A.V. Rahul, Y. Tao, F. Van Bockstaele, K. Dewettinck, G. Ye, G. De Schutter, Rheology of alkali-activated slag pastes: new insight from microstructural investigations by cryo-SEM, Cement Concr. Res. 157 (2022) 106806, https://doi.org/10.1016/j.cemconres.2022.106806.

[46] Y. Tao, M.K. Mohan, A.V. Rahul, Y. Yuan, G. De Schutter, K. Van Tittelboom, Stiffening controllable concrete modified with redispersible polymer powder for twin-pipe printing, Cement Concr. Res. 161 (2022) 106953, https://doi.org/10.1016/j.cemconres.2022.106953.

[47] S. Ghorbani, L. Stefanini, Y. Sun, B. Walkley, J.L. Provis, G. De Schutter, S. Matthys, Characterisation of alkali-activated stainless steel slag and blast-furnace slag cements, Cem. Concr. Compos. 143 (2023) 105230.

[48] Y. Sun, Y. Tao, A.V. Rahul, G. Ye, G. De Schutter, Effect of high-range water-reducing admixtures on alkali-activated slag concrete, ACI Mater. J. (2022), https://doi.org/10.14359/51737192.

[49] M.M. Alonso, S. Gismera, M.T. Blanco, M. Lanzón, F. Puertas, Alkali-activated mortars: workability and rheological behaviour, Construct. Build. Mater. 145 (2017) 576–587, https://doi.org/10.1016/j.conbuildmat.2017.04.020.

[50] H. Alghamdi, S.A.O. Nair, N. Neithalath, Insights into material design, extrusion rheology, and properties of 3D-printable alkali-activated fly ash-based binders, Mater. Des. 167 (2019) 107634, https://doi.org/10.1016/j.matdes.2019.107634.

[51] P. Chindaprasirt, T. Phoo-ngernkham, S. Hanjitsuwan, S. Horpibulsuk, A. Poowancum, B. Injorhor, Effect of calcium-rich compounds on setting time and strength development of alkali-activated fly ash cured at ambient temperature, Case Stud. Constr. Mater. 9 (2018) e00198.

[52] M.K. Mohan, A. V Rahul, Y. Tao, G. De Schutter, K. Van Tittelboom, Hydration re-initiation of borated CSA systems with a two-stage mixing process: an application in extrusion-based concrete 3D printing, Cement Concr. Res. 159 (2022) 106870.

[53] L. Wadsö, Operational issues in isothermal calorimetry, Cement Concr. Res. 40 (2010) 1129–1137.

[54] D.L. Bish, S.A. Howard, Quantitative phase analysis using the Rietveld method, J. Appl. Crystallogr. 21 (1988) 86–91.

[55] G. Álvarez-Pinazo, A. Cuesta, M. García-Maté, I. Santacruz, E.R. Losilla, A.G. De la Torre, L. León-Reina, M.A.G. Aranda, Rietveld quantitative phase analysis of Yeelimite-containing cements, Cement Concr. Res. 42 (2012) 960–971.

[56] F. Bullerjahn, D. Schmitt, M. Ben Haha, Effect of raw mix design and of clinkering process on the formation and mineralogical composition of (ternesite) belite calcium sulphoaluminate ferrite clinker, Cement Concr. Res. 59 (2014) 87–95.

[57] R.P. Chhabra, J.F. Richardson, Non-Newtonian fluid behaviour, Non-Newtonian Flow Appl. Rheol. (2008) 1–55.

[58] P.F.G. Banfill, Rheological methods for assessing the flow properties of mortar and related materials, Construct. Build. Mater. 8 (1994) 43–50, https://doi.org/10.1016/0950-0618(94)90007-8.

[59] F. Puertas, B. González-Fonteboa, I. González-Taboada, M.M. Alonso, M. Torres-Carrasco, G. Rojo, F. Martínez-Abella, Alkali-activated slag concrete: fresh and hardened behaviour, Cem. Concr. Compos. (2018), https://doi.org/10.1016/j.cemconcomp.2017.10.003.

[60] U. Pott, D. Stephan, Penetration test as a fast method to determine yield stress and structural build-up for 3D printing of cementitious materials, Cem. Concr. Compos. 121 (2021) 104066.

[61] D. Lootens, P. Jousset, L. Martinie, N. Roussel, R.J. Flatt, Yield stress during setting of cement pastes from penetration tests, Cement Concr. Res. 39 (2009) 401–408.

[62] Z. Zhang, X. Yao, H. Zhu, Potential application of geopolymers as protection coatings for marine concrete: II. Microstructure and anticorrosion mechanism, Appl. Clay Sci. 49 (2010) 7–12.

[63] W.S. Alyhya, S. Kulasegaram, B.L. Karihaloo, Simulation of the flow of self-compacting concrete in the V-funnel by SPH, Cement Concr. Res. 100 (2017) 47–59.

[64] Product Specification, (n.d.).

[65] G. Vantyghem, W. De Corte, E. Shakour, O. Amir, 3D printing of a post-tensioned concrete girder designed by topology optimization, Autom. ConStruct. 112 (2020) 103084.

[66] J. Newman, B.S. Choo, Advanced Concrete Technology 2: Concrete Properties, Elsevier, 2003.

[67] Y. Sun, L. Miranda, D. Lima, L. Rossi, D. Jiao, Z. Li, G. Ye, G. De Schutter, Cement and Concrete Research Interpretation of the early stiffening process in alkali-activated slag pastes, Cement Concr. Res. 167 (2023) 107118, https://doi.org/10.1016/j.cemconres.2023.107118.

[68] C. Shi, R.L. Day, A calorimetric study of early hydration of alkali-slag cements, Cement Concr. Res. 25 (1995) 1333–1346.

[69] Y. Tao, M.K. Mohan, A. V Rahul, G. De Schutter, K. Van Tittelboom, Development of a calcium sulfoaluminate-Portland cement binary system for twin-pipe 3D concrete printing, Cem. Concr. Compos. 138 (2023) 104960.

[70] M. Ben Haha, B. Lothenbach, G. Le Saout, F. Winnefeld, Influence of slag chemistry on the hydration of alkali-activated blast-furnace slag - Part I: effect of MgO, Cement Concr. Res. 41 (2011) 955–963, https://doi.org/10.1016/j.cemconres.2011.05.002.

[71] C. Kulasuriya, V. Vimonsatit, W.P.S. Dias, P. De Silva, Design and development of alkali pozzolan cement (APC), Construct. Build. Mater. 68 (2014) 426–433.

[72] M. Ben Haha, G. Le Saout, F. Winnefeld, B. Lothenbach, Influence of activator type on hydration kinetics, hydrate assemblage and microstructural development of alkali activated blast-furnace slags, Cement Concr. Res. 41 (2011) 301–310, https://doi.org/10.1016/j.cemconres.2010.11.016.

[73] F. Puertas, A. Fernández-Jiménez, M.T. Blanco-Varela, Pore solution in alkali-activated slag cement pastes. Relation to the composition and structure of calcium silicate hydrate, Cement Concr. Res. 34 (2004) 139–148.

[74] V.L. Bonavetti, V.F. Rahhal, E.F. Irassar, Studies on the carboaluminate formation in limestone filler-blended cements, Cement Concr. Res. 31 (2001) 853–859.

[75] S. Aydın, B. Baradan, Effect of activator type and content on properties of alkali-activated slag mortars, Compos. Part B Eng. 57 (2014) 166–172.

[76] Z. Zhang, L. Li, X. Ma, H. Wang, Compositional, microstructural and mechanical properties of ambient condition cured alkali-activated cement, Construct. Build. Mater. 113 (2016) 237–245.

[77] A.R. Brough, A. Atkinson, Sodium silicate-based, alkali-activated slag mortars: Part I. Strength, hydration and microstructure, Cement Concr. Res. 32 (2002) 865–879.

[78] W. Kunther, S. Ferreiro, J. Skibsted, Influence of the Ca/Si ratio on the compressive strength of cementitious calcium–silicate–hydrate binders, J. Mater. Chem. A 5 (2017) 17401–17412.

[79] G. Le Saoût, M. Ben Haha, F. Winnefeld, B. Lothenbach, Hydration degree of alkali-activated slags: a 29 Si NMR study, J. Am. Ceram. Soc. 94 (2011) 4541–4547.

[80] M. Ben Haha, B. Lothenbach, G.L. Le Saout, F. Winnefeld, Influence of slag chemistry on the hydration of alkali-activated blast-furnace slag—Part I: effect of MgO, Cement Concr. Res. 41 (2011) 955–963.

[81] Z. Wang, S. Park, H.R. Khalid, H.K. Lee, Hydration properties of alkali-activated fly ash/slag binders modified by MgO with different reactivity, J. Build. Eng. 44 (2021) 103252.

[82] G. Kim, S. Im, H. Jee, H. Suh, S. Cho, M. Kanematsu, S. Morooka, T. Koyama, Y. Nishio, A. Machida, Effect of magnesium silicate hydrate (MSH) formation on the local atomic arrangements and mechanical properties of calcium silicate hydrate (CSH): in situ X-ray scattering study, Cement Concr. Res. 159 (2022) 106869.

[83] T. Yang, Z. Zhang, H. Zhu, X. Gao, C. Dai, Q. Wu, Re-examining the suitability of high magnesium nickel slag as precursors for alkali-activated materials, Construct. Build. Mater. 213 (2019) 109–120.

[84] D. Wan, H. Liu, X. Zhao, J. Qu, S. Xiao, Y. Hou, Role of the Mg/Al atomic ratio in hydrotalcite-supported Pd/Sn catalysts for nitrate adsorption and hydrogenation reduction, J. Colloid Interface Sci. 332 (2009) 151–157.

[85] M. Ben Haha, B. Lothenbach, G. Le Saout, F. Winnefeld, Influence of slag chemistry on the hydration of alkali-activated blast-furnace slag - Part II: effect of Al2O3, Cement Concr. Res. 42 (2012) 74–83, https://doi.org/10.1016/j.cemconres.2011.08.005.

[86] M. Vespa, E. Wieland, R. Dähn, D. Grolimund, A.M. Scheidegger, Determination of the elemental distribution and chemical speciation in highly heterogeneous cementitious materials using synchrotron-based micro-spectroscopic techniques, Cement Concr. Res. 37 (2007) 1473–1482.

[87] S.R. Gislason, E.H. Oelkers, Mechanism, rates, and consequences of basaltic glass dissolution: II. An experimental study of the dissolution rates of basaltic glass as a function of pH and temperature, Geochem. Cosmochim. Acta 67 (2003) 3817–3832.

[88] J.L. Provis, J.S.J. Van Deventer, RILEM State-Of-The-Art Reports State-Of-The-Art Report, RILEM TC 224-AAM, n.d..

[89] J.L. Provis, S.A. Bernal, Geopolymers and related alkali-activated materials, Annu. Rev. Mater. Res. 44 (2014) 299–327, https://doi.org/10.1146/annurev-matsci-070813-113515.

[90] F. Puertas, A. Fernández-Jiménez, M.T. Blanco-Varela, Pore solution in alkali-activated slag cement pastes. Relation to the composition and structure of calcium silicate hydrate, Cement Concr. Res. 34 (2004) 139–148, https://doi.org/10.1016/S0008-8846(03)00254-0.

[91] R. Cao, S. Zhang, N. Banthia, Y. Zhang, Z. Zhang, Interpreting the early-age reaction process of alkali-activated slag by using combined embedded ultrasonic measurement, thermal analysis, XRD, FTIR and SEM, Compos. Part B Eng. 186 (2020) 107840, https://doi.org/10.1016/j.compositesb.2020.107840.